iScience

CellPress
OPEN ACCESS

Article

Use of metamodels for rapid discovery of narrow bandgap oxide photocatalysts

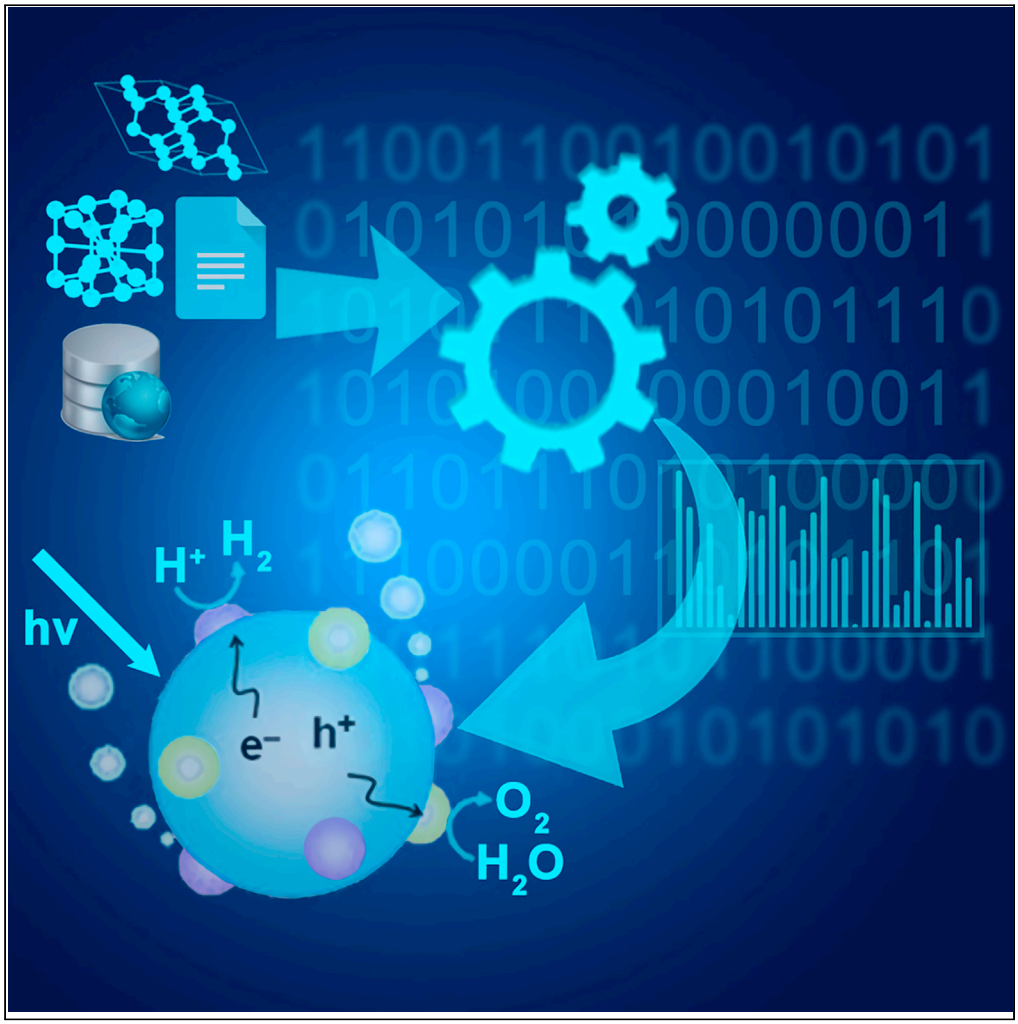

Haoxin Mai, Tu C. Le, Takashi Hisatomi, Dehong Chen, Kazunari Domen, David A. Winkler, Rachel A. Caruso

dehong.chen@rmit.edu.au (D.C.)
david.winkler@monash.edu (D.A.W.)
rachel.caruso@rmit.edu.au (R.A.C.)

Highlights

Stacking models predict bandgap and H_2 evolution activity of oxide photocatalysts

Models predict robustly across a wide range of material structures

Models rapidly identify promising photocatalysts from 10 million materials

Four compounds are synthesized and confirm predicted results

Mai et al., iScience *24*, 103068
September 24, 2021
https://doi.org/10.1016/j.isci.2021.103068

iScience

CellPress
OPEN ACCESS

Article

Use of metamodels for rapid discovery of narrow bandgap oxide photocatalysts

Haoxin Mai,[1] Tu C. Le,[2] Takashi Hisatomi,[3] Dehong Chen,[1,*] Kazunari Domen,[3,4] David A. Winkler,[5,6,7,*] and Rachel A. Caruso[1,8,*]

SUMMARY

New photocatalysts are traditionally identified through trial-and-error methods. Machine learning has shown considerable promise for improving the efficiency of photocatalyst discovery from a large potential pool. Here, we describe a multi-step, target-driven consensus method using a stacking meta-learning algorithm that robustly predicts bandgaps and H_2 evolution activities of photocatalysts. Trained on small datasets, these models can rapidly screen a large space (>10 million materials) to identify promising, non-toxic compounds as candidate water splitting photocatalysts. Two effective compounds and two controls possessing optimal bandgap values (~2 eV) but not photoactivity as predicted by the models were synthesized. Their experimentally measured bandgaps and H_2 evolution activities were consistent with the predictions. Conspicuously, the two compounds with strong photoactivities under UV and visible light are promising visible-light-driven water splitting photocatalysts. This study demonstrates the power of machine learning and the potential of big data to accelerate discovery of next-generation photocatalysts.

INTRODUCTION

The ever-increasing need for energy and the clear environmental impact of fossil fuels in the 21st century are driving a rapid move to renewable energy sources (Furlan and Mortarino, 2018; Meinshausen et al., 2009; Wang et al., 2015). Of these, solar energy is the most attractive because the sun provides free, renewable, abundant, and sustainable energy at a rate of ~1 kW/m^2 (Green and Bremner, 2017; Kannan and Vakeesan, 2016). An attractive way to store solar energy is through photocatalytic water splitting, producing hydrogen as clean chemical fuel from water by sunlight (Chen et al., 2017; Tachibana et al., 2012; Wang and Domen, 2020; Wang et al., 2015; Zhang et al., 2016). Since the discovery of the photocatalytic properties of TiO_2 in 1972 (Fujishima and Honda, 1972), more than 140 types of inorganic photocatalysts have been discovered (Chen et al., 2019; Lee and Choi, 2018; Nursam et al., 2015; Pan et al., 2018; Wang and Domen, 2020; Wang et al., 2014, 2015, 2018, 2019b; Zhang et al., 2016). However, the large bandgaps or poor matching of the redox potentials of most photocatalysts results in low quantum efficiency and poor catalytic water splitting activity under visible light, hampering commercial applications (Kudo and Miseki, 2009). Clearly, much more effective photocatalysts are required to make solar hydrogen production commercially viable.

High-efficiency photocatalysts must satisfy two basic criteria. Firstly, although the free energy barrier for water splitting is 1.23 eV per electron, a bandgap of ~2 eV is necessary for photocatalysts to trigger the water splitting reactions because of overpotentials, device operating voltage, and other losses (Zhu and Wang, 2017). Secondly, photocatalysts must have redox potentials that match the reaction, i.e., their conduction band minimum must be more negative than the H^+/H_2 potential (Wang and Domen, 2020). To discover materials that match these criteria, the traditional laboratory-based trial-and-error method has largely been used to discover suitable materials, albeit with low efficiencies and high cost. With the impressive developments in computing technologies and high-throughput combinatorial techniques, high-throughput screening based on density functional theory (DFT) has become feasible for investigating functional materials, including photocatalysts (Castelli et al., 2015; Davies et al., 2016; Wu et al., 2013; Zhang et al., 2018). A vast amount of data produced by these investigations has been collected in databases such as The Materials Project, providing electronic structures and thermodynamic information for

[1]Applied Chemistry and Environmental Science, School of Science, STEM College, RMIT University, GPO Box 2476, Melbourne, VIC 3001, Australia

[2]School of Engineering, STEM College, RMIT University, GPO Box 2476, Melbourne, VIC 3001, Australia

[3]Research Initiative for Supra-Materials (RISM), Shinshu University, 4-17-1 Wakasato, Nagano 380-8553, Japan

[4]Office of University Professors, the University of Tokyo, 2-11-16 Yayoi, Bunkyo-ku, Tokyo 113-8656, Japan

[5]Monash Institute of Pharmaceutical Sciences, Monash University, Parkville, VIC 3052, Australia

[6]School of Biochemistry and Genetics, La Trobe University, Kingsbury Drive, 3042 Bundoora, Australia

[7]School of Pharmacy, University of Nottingham, NG7 2RD Nottingham, UK

[8]Lead contact

*Correspondence: dehong.chen@rmit.edu.au (D.C.), david.winkler@monash.edu (D.A.W.), rachel.caruso@rmit.edu.au (R.A.C.)

https://doi.org/10.1016/j.isci.2021.103068

materials researchers (Wang et al., 2016). Despite these achievements, the complexity of photocatalysts increases the computational cost of predicting the photocatalytic properties, and size of material space extends the screening time, resulting in low screening efficiency (Tabor et al., 2018). Until recently, even the most advanced high-throughput ab initio simulations were only tractable for a few thousand compounds, an infinitesimal fraction of the chemically accessible materials space (Davies et al., 2016). However, increases in computational hardware and algorithms have seen DFT calculations being performed for up to 1 million materials (Chanussot et al., 2021).

Advanced materials informatics and artificial intelligence provide an alternative means of tackling this dilemma (Butler et al., 2018; Jordan and Mitchell, 2015; Le et al., 2012; Sanchez-Lengeling and Aspuru-Guzik, 2018; Tabor et al., 2018). In particular, machine learning (ML) techniques have made rapid progress in the design of diverse materials such as organic-inorganic perovskites, metal-organic frameworks, phosphors, catalysts, and metallic glasses (Fanourgakis et al., 2020; Gómez-Bombarelli et al., 2016; Gu et al., 2019; Lu et al., 2018; Ren et al., 2018; Sun et al., 2020; Zhuo et al., 2018). ML models trained on a relatively small number of expensive first principles electronic structure calculations can predict a myriad of electronic, physical, and mechanical properties, such as formation energies, gas uptake, bulk and shear modulus, and bandgap (Chen et al., 2020; Himanen et al., 2019; Toyao et al., 2020). Furthermore, by applying feature engineering to these ML models, complicated feature-property relationships can be identified without any prior knowledge of the materials system (Tabor et al., 2018). For these reasons, ML models are becoming widely used for identifying new materials with bespoke properties from extremely large materials spaces.

Although ML techniques have been used to model existing photocatalyst properties, their use to discover new photocatalysts is still relatively uncommon (Can and Yildirim, 2019; Fathinia et al., 2016). There are two main problems in applying ML to photocatalyst design (Masood et al., 2019). One issue is that the structural diversity of photocatalytic materials is quite high. Most ML models are trained on small subsets of chemically similar materials, and these models have relatively small domains of applicability. They are therefore not capable of making accurate predictions of properties of materials in large photocatalyst databases. Another problem is that experimental photocatalysis data are relatively inconsistent. For example, H_2 evolution rates are acquired in a range of reaction environments using different measurement protocols. The method of preparation can also affect photocatalytic properties. However, if all these experimental data are captured, they can be useful features for training ML models.

To address these challenges and provide fast computational screening of large databases to discover novel and efficient water splitting photocatalysts, here we describe a multi-step, target-driven modeling approach for discovery of narrow bandgap, non-toxic photocatalysts. Separate meta-learning ML models were generated for the bandgap and hydrogen evolution reaction (HER) activity, which are important for photocatalyst performance, using a dataset of chemically diverse photocatalysts. The meta-learning algorithm is a consensus method that uses a stacking algorithm to generate a metamodel from a set of base models. This approach generates robust and predictive bandgap and HER activity models that are superior to the base models. These models were used to search a material space of over one million unexplored materials. To provide initial validation of the utility of the method, four structurally diverse compounds predicted to have narrow bandgaps were synthesized. Subsequent experimental measurements of their bandgaps and HER activity showed excellent agreement with the model predictions. These results exemplify how accelerated design and discovery of novel water splitting photocatalysts may be achieved using ML techniques that require relatively modest computational and experimental resources.

RESULTS AND DISCUSSION

The dataset was randomly partitioned into a training set, 80% of the photocatalysts and a test set, 20% of the photocatalysts used to assess the prediction accuracy of the models. Models with the best performance on the test set were used to screen a large set of untested materials to identify a shortlist predicted to have optimal bandgaps and useful HER activity. These materials were subsequently synthesized and their electronic and photocatalytic properties measured. Materials identified by this computational screening paradigm constitute promising photocatalysts for commercial application. This multi-step, target-driven approach to design of narrow bandgap photocatalysts is depicted in Figure 1.

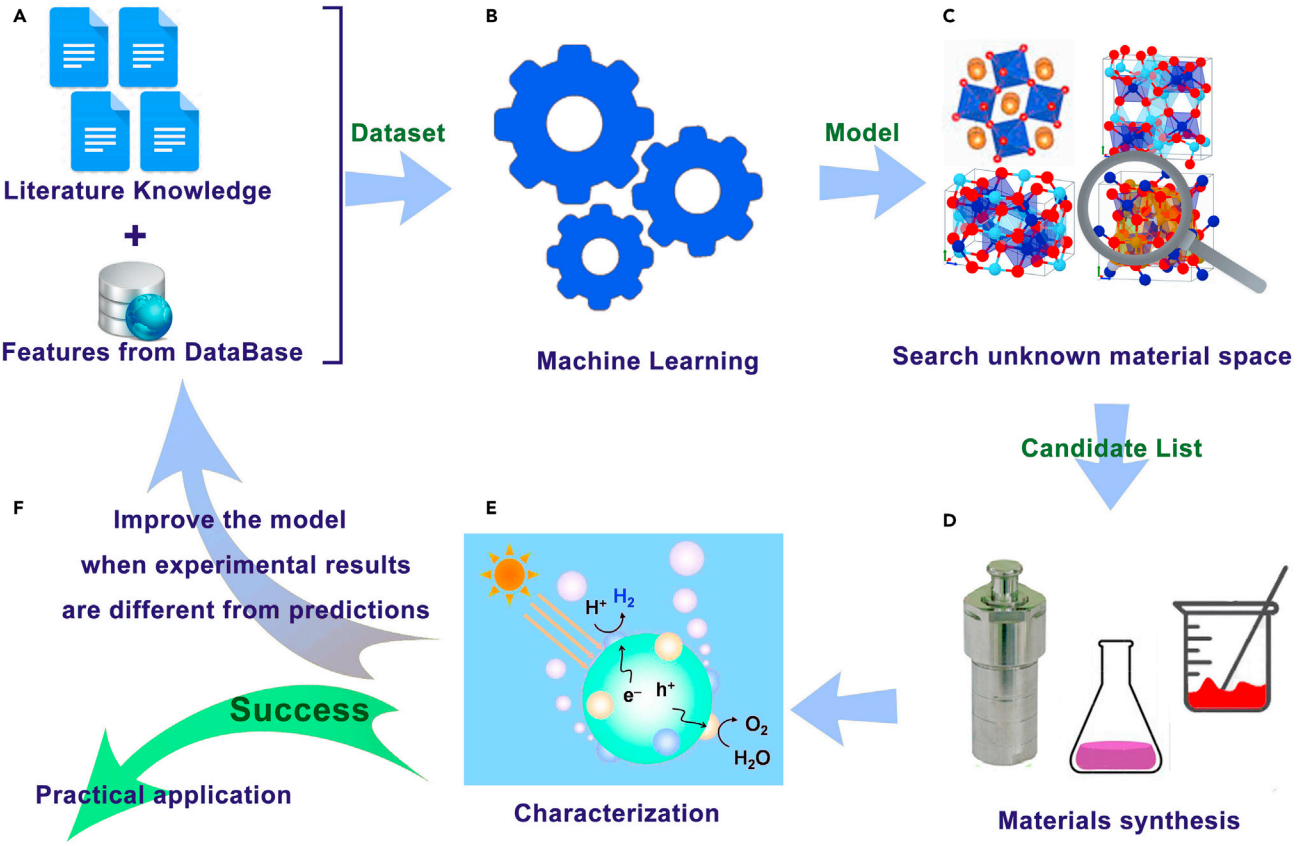

Figure 1. The workflow for target-driven narrow bandgap photocatalyst design

(A) Chemical features and photocatalysis data from the literature were used to build the dataset.

(B) Bandgap regression and HER activity classification ML models were trained on these.

(C) The best ML models were used to scan unknown material space (~10^6 materials), identifying a list of candidates with optimal bandgaps and HER activity.

(D and E) (D) These candidates were synthesized and (E) their bandgap and H_2 evolution measured.

(F) These new experimental data can be added to the dataset to improve subsequent models, closing the loop.

Bandgap regression models

Machine learning base models

Most ML algorithms are capable of generating high-performance models that predict material properties and elucidate property-structure relationships (Butler et al., 2018; Chen et al., 2020; Gu et al., 2019; Tabor et al., 2018; Toyao et al., 2020). The largest performance differences are seen between linear and nonlinear models. Least absolute shrinkage and selection operator (LASSO), kernel ridge regression (KRR), artificial neural networks, support vector regression (SVR), random forest (RF), extra tree (EXT), and different types of gradient boosting regression (GBR) have been used to predict the bandgap of diverse compounds (Li et al., 2019, 2020a; Lu et al., 2018). Although these models could recapitulate the properties of photocatalysts well, two problems remain. Some models were trained on bandgaps calculated by DFT methods known to underestimate them (Wang and Pickett, 1983). Secondly, most models are trained on photocatalysts with limited chemical diversity. The small domains of applicability of these models compromises their abilities to predict photocatalytic properties for materials with a much wider range of structures such as perovskites, scheelites, spinels, and others (Wang and Domen, 2020).

We first generated ML models for photocatalyst bandgap prediction using 10 popular ML algorithms: RF, EXT, GBR, KRR, LASSO, ridge regression (Ridge), and SVR algorithms with radial basis function (SVR(rbf)), polynomial (SVR(poly)), and linear (SVR(linear)) kernels. Three metrics were used together to assess the performance of models: the coefficient of determination (R^2), root mean squared error (RMSE), and mean absolute error (MAE). The latter two measures of dispersion are preferred over R^2 values as they

Table 1. Performance of various models on the bandgap predictions on the BG dataset

Models	R^2	RMSE [eV]	MAE [eV]	t-value/p value
SVR(rbf)	0.94/0.81	0.26 ± 0.00/0.47 ± 0.00	0.19 ± 0.00/0.32 ± 0.00	3.72/0.021
SVR(poly)	0.61/0.58	0.61 ± 0.00/0.63 ± 0.00	0.51 ± 0.00/0.60 ± 0.00	4.91/0.008
SVR(linear)	0.46/0.38	0.73 ± 0.00/0.74 ± 0.00	0.62 ± 0.00/0.72 ± 0.00	5.77/0.004
LASSO	0.51/0.46	0.69 ± 0.00/0.71 ± 0.00	0.66 ± 0.00/0.72 ± 0.00	5.47/0.005
Ridge	0.51/0.45	0.69 ± 0.00/0.71 ± 0.00	0.67 ± 0.00/0.72 ± 0.00	5.57/0.005
KRR	0.92/0.82	0.46 ± 0.00/0.71 ± 0.00	0.23 ± 0.00/0.35 ± 0.00	5.05/0.007
RF	0.94/0.87	0.30 ± 0.02/0.37 ± 0.05	0.18 ± 0.01/0.28 ± 0.02	11.5/0.0003
EXT	0.94/0.88	0.28 ± 0.02/0.38 ± 0.05	0.20 ± 0.01/0.30 ± 0.02	9.55/0.0007
GBR	0.99/0.87	0.10 ± 0.02/0.35 ± 0.05	0.06 ± 0.01/0.30 ± 0.02	9.30/0.0007

Results are reported as training set/test set, RMSE and MAE are acquired from the average of 100 times training/testing. Paired sample t test is carried out between one base-model and STRBG model on RMSE, degrees of freedom is 5 and the pre-selected level of significance is 0.05.

are not dependent on the number of data points and number of parameters in the model (Alexander et al., 2015). MAE values are less biased by one or two large outliers in the predictions than RMSE values.

The linear regression models (e.g. LASSO, Ridge, SVR(linear)) performed poorly in predicting the BG values for the test set (Table 1). The nonlinear RF, EXT, and GBR methods generated relatively accurate predictions of the test set bandgap values (MAE values of ~0.3 eV for the test set). The performance of these models is illustrated graphically in Figure S3.

Consensus metamodeling stacking algorithm approach

Despite the nonlinear models having good performance, none of them recapitulated the reported bandgaps to within the estimated experimental error of ±0.2 eV. The residual prediction error may result from the use of a small number of features and the wide diversity of materials in this dataset. In such cases, a hybrid (consensus) model may be more successful in predicting the photocatalytic properties of all materials in the dataset.

We employed a stacking algorithm that creates an ensemble of ML models to make more accurate predictions of the properties under study (Wolpert, 1992). Stacking aims to achieve generalization accuracy, rather than a learning accuracy, that is as high as possible. Unlike other consensus models, stacked generalization deduces the biases of the models with respect to a given training set. Stacking involves training a learning algorithm that combines the predictions of several other learning algorithms. The other (base) algorithms are trained first using the available data, then a combiner algorithm is trained on all predictions of the base algorithms as additional inputs to generate a metamodel that is more accurate than any of the base models. In theory, if an arbitrary combiner algorithm is used, then stacking can represent any type of ensemble learning (Chatzimparmpas et al., 2021; Ghasemian et al., 2020; Ma et al., 2018; Singh et al., 2019; Wang, 2018). Stacking is a possible solution to the problems posed by small datasets (Butler et al., 2018).

Figure 2 summarizes the architecture of the stacking model used in this work. It consists of two levels. At the base level, several ML algorithms are chosen, and each algorithm generates 5 models from the training datasets using 5-fold cross validation. The outputs of these base models are used as the features (meta-features) to train the metamodel in the next level. When the metamodel is trained by an appropriate algorithm, it results in the best combination of the base models for bandgap prediction of different types of materials (see Figure S4).

Based on the preliminary ML models for the bandgap (Table 1), we selected six nonlinear algorithms, RF, EXT, GBR, KRR, SVR(rbf), and SVR(poly), as the base models. The poorly performing linear algorithms were not used. The final bandgap stacking model (STR_{BG}) was trained using the SVR(rbf) algorithm. The R^2, RMSE, and MAE of the STR_{BG} model was 0.97, 0.16 ± 0.03 eV, and 0.11 ± 0.02 eV, respectively, for the test set, close to the values for the training set prediction and the estimated experimental error. This suggested that the model was robust and not overfitted (Figure 3A). Comparison with the single ML models of bandgap predictions listed in Table 1 shows that the STR_{BG} model outperformed all other models (the best set RMSE value for the GBR models being 0.35 ± 0.05 eV). A paired t test showed that these RMSE values were different at the 99.7% confidence level.

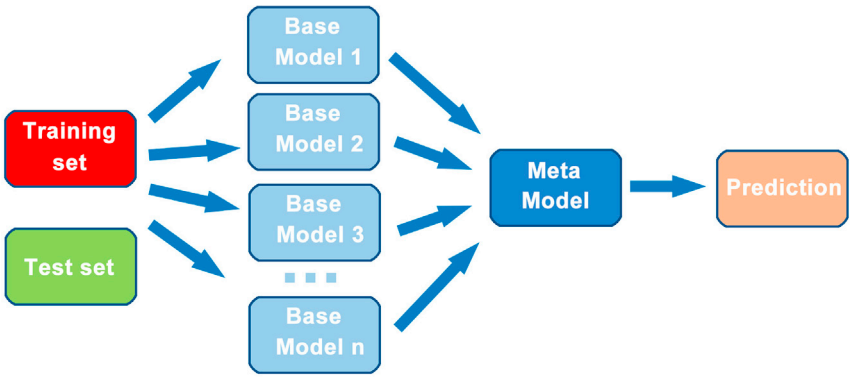

Figure 2. The architecture of the 2-level stacking model

Each of the n base models consists of five weak models generated by 5-fold cross validation. The outputs of the base models for the training data were meta-features used to train a meta-model that finds the best combination of the base models for each input. The test set predictions of specific base models were averages (for regression) or votes (for classifiers) of the predictions from the weak models.

The contributions of features to the bandgap model were estimated by GBR, the best performing base model algorithm for this dataset. As Figure 3B shows, the most important contributors to the bandgap model are R_B, X_B, and E_A, reinforcing the importance of both components A and B on the bandgap. Although there was no simple relationship between features and bandgap, the model suggested that the oxides with optimal bandgap for water splitting are most likely to possess R_B in the range of 240–250 pm, X_B in the range of 1.5–2.2, and E_A > 520 kJ mol^{-1} (Figure S5). In other words, the oxides with optimal bandgap for water splitting are not likely to contain Al, Zr, Nb, or Bi at the B-site and an alkali metal element at the A-site of these oxides.

To evaluate the performance of the STR_{BG} model across a range of materials, 10 compounds not included in the BG dataset were extracted from the literature (Table 2) (Adak et al., 2020; Bai et al., 2012; Bouzidi et al., 2010; Maeda et al., 2020; Vavilapalli et al., 2018; Wheeler and Choi, 2018; Wu et al., 2012, 2017). These compounds are mainly used in electronic and magnetic devices and are not primarily photocatalysts. The predicted bandgap values from the STR_{BG} model and the experimental values from the literature are listed in Table 2. The MAE between the predicted value and the reported value was 0.17 eV, and the maximum error was −0.35 eV for $Bi_6Ti_3Fe_2O_{18}$. The table shows that the STR_{BG} metamodel is clearly the most reliable for predicting the reported bandgaps, with all predictions within 10%. This preliminary validation study suggests that the STR_{BG} model makes useful bandgap predictions for unknown compounds with diverse structures (see also Table S5).

H_2 evolution classification models

H_2 evolution experiments have been conducted using a range of conditions in different laboratories. For example, incident light, solutions, and co-catalysts used to boost H_2 evolution vary, and the morphology,

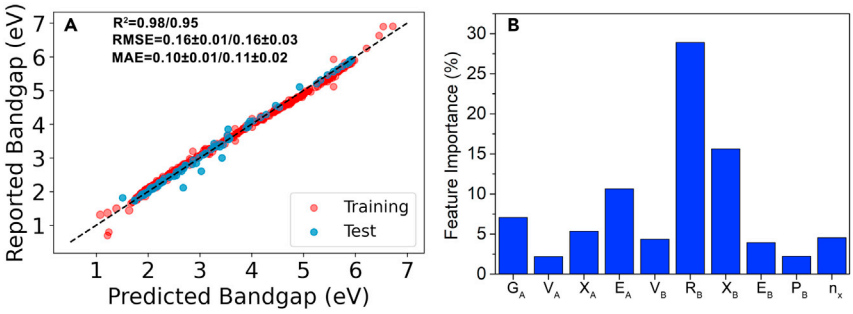

Figure 3. Performance of bandgap regression models

(A) The bandgap of the photocatalysts in the BG dataset predicted by STR_{BG} model versus reported bandgap values. The R^2, RMSE, and MAE were for the training set/test set. RMSE and MAE are acquired from the average of 100 times training/testing.
(B) Relative importance of top 10 features from the GBR bandgap model.

Table 2. Predictions of the bandgap (eV) of the 10 unknown samples from base and metamodels

Material	STR_{BG}	RF	GBR	EXT	KRR	SVR(rbf)	SVR (poly)	Reported bandgap
$(Ba_{0.5}Ni_{0.5})Bi_2NbTaO_9$	2.72	3.16	3.14	2.92	2.98	2.69	2.94	2.55
$Bi_2Ti_4O_{11}$	2.80	2.90	2.99	2.87	2.56	1.97	2.51	3.10
$Bi_5Ti_3FeO_{15}$	2.25	2.43	2.15	2.17	2.07	1.67	1.98	2.03
$Bi_6Ti_3Fe_2O_{18}$	3.37	2.42	2.15	2.17	2.57	3.06	1.55	3.72
$Ca_2Fe_2O_5$	2.22	2.43	2.00	2.14	2.22	2.06	2.39	2.10
$LiVO_3$	3.34	3.15	3.41	2.92	3.38	2.88	3.56	3.30
$KBiFe_2O_5$	1.88	3.34	1.70	2.60	3.48	3.18	3.31	1.68
$SrBi_2Nb_2O_9$	2.66	3.33	3.25	3.44	2.69	2.64	2.47	2.70
$Sr_{0.99}Bi_{2.01}Nb_{1.99}Ni_{0.01}O_{8.99}$	2.50	3.34	3.24	3.35	2.98	2.71	2.32	2.45
$Sr_{0.91}Bi_{2.09}Nb_{1.91}Ni_{0.09}O_{8.91}$	2.48	3.34	3.24	3.39	2.99	2.69	2.30	2.25
Predictions within 10%	10	1	4	3	3	3	1	

size, and surface area of the photocatalysts also differ. This makes it difficult to generate regression models of HER activity trained on the intrinsic properties of the photocatalysts alone: additional descriptors encoding differences in measurement protocols are required, but these are rarely recorded. To overcome this shortcoming, we used classification rather than regression methods to model the HER activity of photocatalysts in this work. We trained classification models on the same features used to train the bandgap regression models. We quantified the quality of predictions of the classification models using accuracy, F1 score, and the area under the receiver operating characteristic curve (AUC) metrics. The latter two metrics are suitable for unbalanced classification models where one class is more highly represented than the other. To improve the prediction accuracy, three ensemble algorithms, RF, EXT, and gradient boosting trees (GBTs), were applied, and three bagging models derived from 100 SVM classifiers with RBF, polynomial, and linear kernels were constructed. The results of these six classification models were used to train a stacking metamodel, using the EXT algorithm to form a stacking classifier (STC_{H2} I) (Figure 2). The results of modeling the HER activity using the 6 base algorithms and the stacking algorithm are summarized in Table 3.

The 6 base algorithm models had almost identical AUC and F1 score accuracies of 82 $\pm$ 1%. Although the stacking model showed significantly better prediction accuracy (87-90%) for the test set compared with the six base models, its modest accuracy (Table 3 and Figure S6) suggested that additional chemical features may improve the accuracy of the H_2 evolution activity metamodel. For H_2 evolution to occur, the H^+ in the solution must capture the photoelectrons at the surface of the photocatalyst. As this reaction is strongly affected by the band structure of the photocatalyst, we hypothesized that the bandgap may be a useful additional feature for the H_2 evolution metamodel. Therefore, we added the experimental bandgaps or those predicted by the STR_{BG} model if experimental bandgaps were not available to the training set. The six base classifiers were retrained, and a second stacking classifier for H_2 evolution activity (STC_{H2} II) was generated.

Interestingly, as Table 4 and Figure S7 show, the test set prediction accuracy was only significantly improved for the three bagging models, with the other three algorithms providing slight improvement

Table 3. Performance of the six base and stacking metamodels on the H_2 activity classification without bandgap descriptor (results are reported as training set/test set)

Models	AUC	Accuracy	F1 score
RF	0.98/0.83	0.94/0.81	0.96/0.81
GBT	0.98/0.80	0.93/0.82	0.96/0.83
EXT	0.96/0.82	0.93/0.81	0.96/0.81
Bagging (SVC-poly)	1.00/0.80	0.97/0.76	0.99/0.82
Bagging (SVC-rbf)	0.97/0.82	0.94/0.75	0.96/0.81
Bagging (SVC-linear)	0.97/0.82	0.94/0.77	0.96/0.83
STC_{H2} I	0.95/0.87	0.96/0.90	0.95/0.90

Table 4. Performance of the six base- and stacking meta-models on the H_2 activity classification with bandgap descriptor (results are reported as training set/test set)

Models	AUC	Accuracy	F1 score
RF	1.00/0.88	0.96/0.83	0.98/0.85
GBT	1.00/0.85	0.95/0.84	0.97/0.86
EXT	0.96/0.84	0.92/0.84	0.96/0.85
Bagging (SVC-poly)	1.00/0.85	0.99/0.82	0.92/0.83
Bagging (SVC-rbf)	1.00/0.87	0.97/0.87	0.98/0.86
Bagging (SVC-linear)	0.91/0.84	0.98/0.82	0.99/0.84
STC_{H2} II	0.99/0.97	0.98/0.96	0.98/0.96

in accuracies compared to the models without bandgap descriptors. When considering both the F1 score and AUC metrics, RF, GBT, and the SVM classifier with an rbf kernel performed better than the other three models. However, the F1 score and AUC for predictions of the test set by the STC_{H2} II metamodel improved significantly to 96-97% (Figure 4A and Table 3). This again suggests the stacking algorithm is providing better model predictions than any of the base model algorithms.

The test set confusion matrix for the STC_{H2} II model, shown as an inset in Figure 4A, summarizes the accuracy of the active and inactive material predictions. The feature importance evaluated by the average score of RF and GBT (Figure S8) is plotted in Figure 4B. The relative importance of features to the GBT and RF models individually is shown in Figures S8A and S8B. The two algorithms provide similar rankings for the most important features. Bandgap is in the top five most important features (the top three being G_A, E_A, and E_B), indicating its relevance to the models. Moreover, on further analysis, we found that a candidate photocatalyst is likely to have H_2 activity if $G_A < 6$, $E_A < 750$ kJ mol^{-1}, $E_B < 700$ kJ mol^{-1}, and bandgap >3 eV (Figure S9). Considering also the results from the STR_{BG} model, photocatalytic oxides with optimal bandgaps may consist of Ca, Sr, Ba, Fe, Co, Ni, Cu, or Ag and rare earth elements at the A-site and Ti, V, Cr, Mn, Mo, or In at the B-site.

HER model validation

Our studies have shown that the bandgap plays an important role in the modeling of HER active photocatalysts. It determines the range of incident light wavelengths that can be absorbed by the photocatalysts and has significant effects on the accurate prediction of H_2 evolution activity via the STC_{H2} II model. The STR_{BG} metamodel is useful for identifying potential photocatalysts in hitherto unexplored materials that lack bandgap information. Taken together, the STC_{H2} II and STR_{BG} metamodels are useful for identifying small bandgap compounds with potential HER activity in visible light.

As a proof of concept, we collected 51 photocatalytic compounds from the literature where the bandgap was not reported or was uncertain (Table S6). These 51 compounds were not in the BG dataset and H_2 dataset (Table S9 BG dataset related to STAR Methods and Table S10 H2 dataset related to STAR Methods), and thus, they are unknown to the models. Models are most useful in making predictions about new materials if they lie in or near its domain of applicability. Hence, we projected the training and test sets and these new materials from a 29-dimensional feature space to a 2D map using the t-SNE algorithm (Figure 5A) (Janet et al., 2019; van der Maaten and Hinton, 2008). This analysis suggests that materials in the new 51 dataset cover a similar feature space to that of the training set and test set. Thus, the STR_{BG} and STC_{H2} II metamodels should predict the bandgaps and HER activities with reasonable accuracy. We used the STR_{BG} model to predict the bandgap for the 51 new materials and employed this as an additional feature in the STC_{H2} II H_2 evolution model. The confusion matrix in Figure 5B summarizes the H_2 evolution prediction results for the new set of materials. Forty eight of 51 compounds were correctly classified (94% accuracy, similar accuracy to that for the test set, 96%). Only 37 compounds were correctly labeled when the bandgap was not included in the descriptor set (73% accuracy, Figure 5C). Again, the addition of bandgap as a descriptor increases the prediction accuracy of the STC_{H2} II model. This preliminary proof of concept shows that screening of narrow bandgap photocatalysts in a large material space using the metamodels is possible.

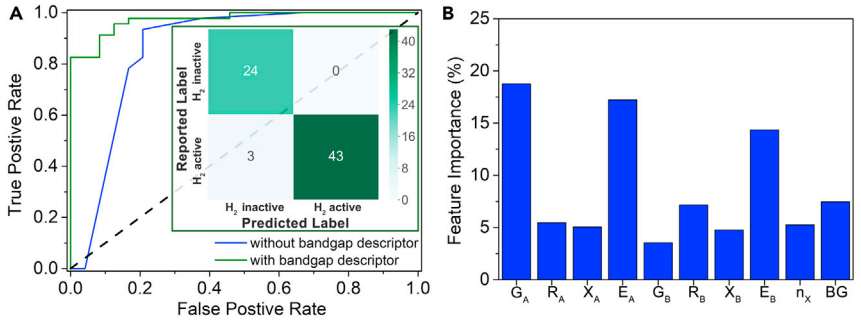

Figure 4. Performance of the H_2 activity stacking classifier

(A) ROC (receiver operating characteristic) curve of the stacking classifier with bandgap descriptor (green line) and without bandgap descriptor (blue line). Inset is the confusion matrix between true label (reported label) and predicted label using the stacking classifier with bandgap descriptor on the test set.

(B) Relative importance of top 10 features from the average score evaluated by GBT and RF classifiers. BG denotes the bandgap descriptor.

Photocatalyst library virtual screening

Given the promising results of the use of stacking metamodels discussed above, they were used to conduct a virtual screen of a large hypothetical library of potential photocatalytic materials to identify those with promising bandgaps and water splitting activities. The framework is illustrated in Figure 6. To ensure the library was close to, or within, the domain of applicability of the models, we divided the metal elements in the periodic table into three regions on the basis of the BG dataset (Table S9 BG dataset related to STAR Methods). Blue regions contain elements that are only found in the A site of materials in the training set, green regions denote elements found solely in the B site, and elements in the red regions are found in either the A or B site. Toxic and rare elements were excluded. An initial library of $> 10^{10}$ electrically neutral compounds with the general formula $A_xA'_{n-x}B_yB'_{m-y}O_l$ ($x > 0$, $x \geq n-x$, $y > 0$, $y \geq m-y$, $l > 0$) was established by combination of 40 A/A′ elements and 23 B/B′ elements. The stability of the host compound of $A_xA'_{n-x}B_yB'_{m-y}O_l$, $A_nB_mO_l$ (where n, m, l must satisfy the electrical neutrality of this compound) was estimated by their formation energy from the Materials Project Database (Jain et al., 2013). Only the materials with negative formation energy were considered to be stable, and the corresponding derivatives $A_xA'_{n-x}B_yB'_{m-y}O_l$ were retained in the dataset. Finally, the number of compounds was reduced by ionic radii screening. This assumes that the A/A′ and B/B′ that can locate at the identical sites in a material have similar ionic radii. Thus, materials in which A/A′ and B/B′ have significantly different ionic radii were removed (e.g., $Ba_{0.5}Sr_{0.5}TiO_3$ could pass the ionic radii screening but $Ba_{0.5}Be_{0.5}TiO_3$ could not). These constraints reduced the number of screening candidates to $\sim 10^6$ and the photocatalytic activity of this set was predicted by the stacking metamodels. The STR_{BG} model was used to predict the bandgaps of the materials, and then, the STC_{H2} II model was used to predict their HER activity. Eventually, we selected the photocatalysts active in visible light (having bandgaps in the range 2.0–2.7 eV).

A short list of ~45,000 oxides was identified to be of visible light HER activity. Based on the novelty and reported synthesis methods (e.g., the selected candidates could be synthesized by the most commonly used methods, such as hydrothermal methods [<200°C], sol-gel methods [common additives, e.g., citric acid, are used and samples are calcined at a temperature <900°C], or solid-state reaction methods [<1500°C, in air and under normal pressure]), we selected 20 candidates from the short list, summarized in Table S7 and Figure S10. To verify the accuracy of this approach, two of the 20 candidates were synthesized, $Bi_9Ti_6FeO_{27}$ and Co_2TiO_4. Two additional compounds in a similar feature space, $CoTi_2O_5$ and $Cu_{0.5}Ni_{0.5}Fe_2O_4$, that were predicted to not generate H_2 but have bandgaps close to the optimal value (~2 eV) were also synthesized as negative controls. The four compounds were pure phases (Figure S11). The experimentally determined bandgaps of these compounds were obtained from the measured UV-vis reflection spectra (Figure S12). These bandgaps were in excellent agreement with the predictions from the STR_{BG} model, with an MAE of 0.03 eV (Figure 7A and Table S8). Conspicuously, HER activity occurred for both $Bi_9Ti_6FeO_{27}$ and Co_2TiO_4 under UV and visible illumination but was absent for $CoTi_2O_5$ and $Cu_{0.5}Ni_{0.5}Fe_2O_4$ under the same conditions (Figures 7B and S13). These results indicate that the predictions of the STR_{BG} model and STC_{H2} II metamodels were useful for virtual screening to identify new photocatalysts from large libraries of candidates.

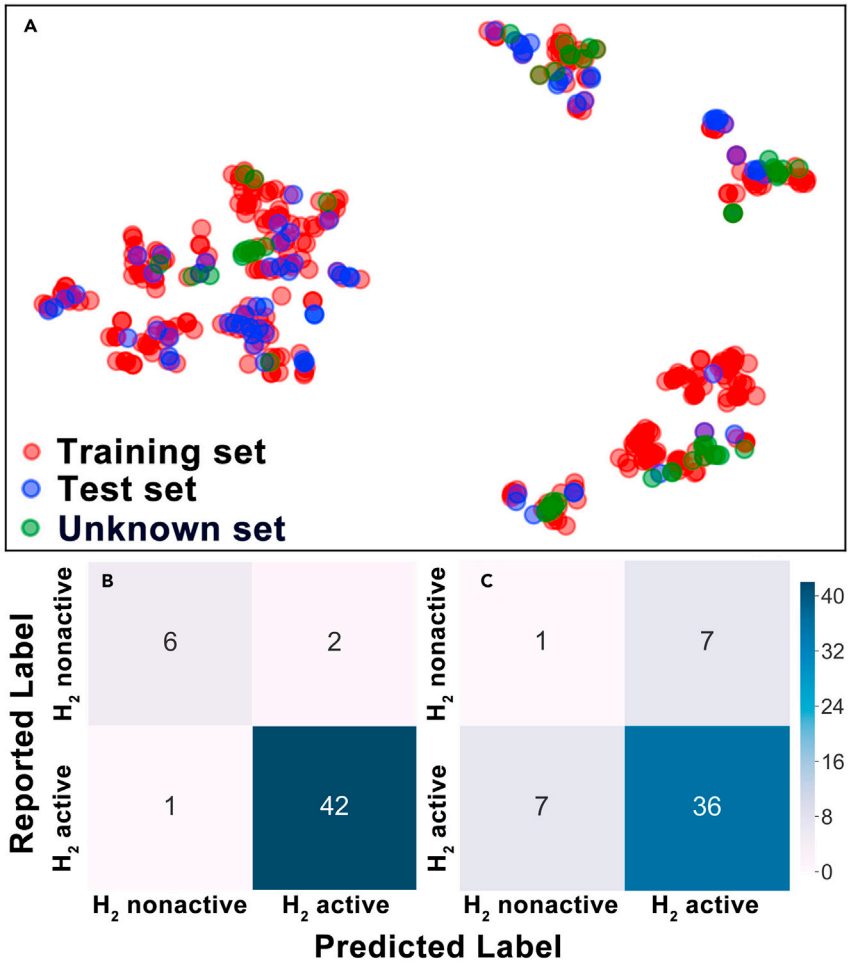

Figure 5. Performance of the combination of STR_{BG} model and SCT_{H2} II model on the unknown dataset

(A–C)(A) Reduced two-dimensional feature space of the training set (red), test set (blue), and unknown set (green) obtained by the t-SNE algorithm. Confusion matrix between true label (reported label) and predicted label using the stacking classifier (B) with bandgap descriptor and (C) without bandgap descriptor on unknown dataset.

Specific structural features of $Bi_9Ti_6FeO_{27}$ and Co_2TiO_4 contributed to their HER activity compared to similar oxides. As a member of Aurivillius phase family (a form of perovskite represented by the general formulae (Bi_2O_2) $(A_{n-1}B_nO_{3n+1})$), $Bi_9Ti_6FeO_{27}$ consists of alternate stacking of $Bi_4Ti_3O_{12}$ and $Bi_5Ti_3FeO_{15}$ layers. As a result, $Bi_9Ti_6FeO_{27}$ showed H_2 evolution activity similar to $Bi_4Ti_3O_{12}$ which has a bandgap of 2.9–3.1 eV (Zhang et al., 2009)). However, it possessed a narrow bandgap (resulting from the $Bi_5Ti_3FeO_{15}$ layer with bandgap of ~2.0 eV (Wu et al., 2012) that does not exhibit H_2 evolution activity). Co_2TiO_4 has a typical inverse spinel structure. Compared to the oxides of similar structure (e.g., CuM_2O_4 (M = Al, Cr, Mn, Fe, and Co), $ZnMn_2O_4$, $ZnFe_2O_4$), electron transfer efficiency was improved by the strong interaction between Co and Ti ions derived from the rigid metal-oxo-metal bridges (Li et al., 2020b), resulting in the HER activity in neutral environment. The metamodel approach identified these two compounds from millions of candidates without having structural information in advance. The H_2 production from $Bi_9Ti_6FeO_{27}$ and Co_2TiO_4 may be improved by optimization of the synthesis conditions, e.g., adjusting reaction time, temperature, and workup methods. Virtual screening of this type allows more time- and resource-intensive experimental and computational resources to be focused on the few most promising materials to further optimize and analyze them.

CONCLUSIONS

A fast, multistep stacking metamodel method has been developed to discover narrow bandgap photocatalysts for water splitting. The metamodels for bandgap and HER activity were more accurate than any of

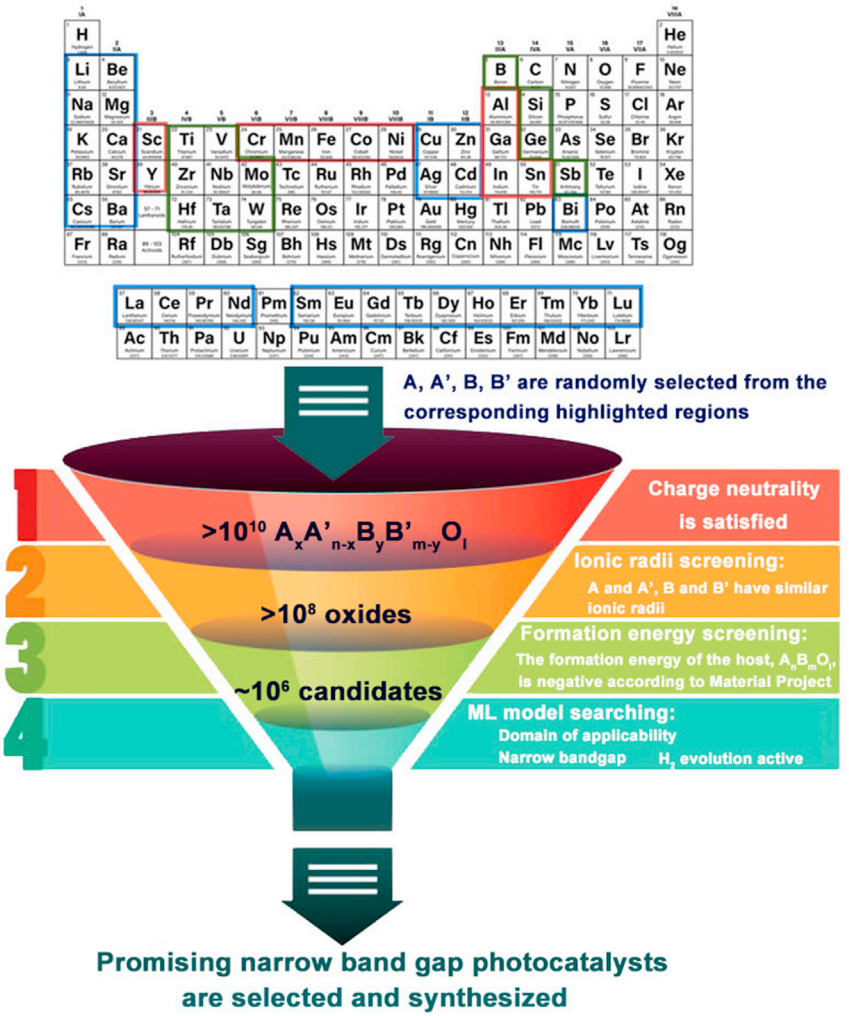

Figure 6. Schematic framework to search for novel photocatalysts ($A_xA'_{n-x}B_yB'_{m-y}O_l$) based on ML models

A, A′, B, and B′ were randomly selected from the corresponding highlighted regions in the periodic table, where the blue highlighted region is for A and A′, green highlighted region is for B and B′, while the elements highlighted red can be selected for A, A′, B, and B′. The combinations of these elements give rise to more than 10^{10} compounds. After screening for charge neutrality, stability, and ionic radii similarity, a candidate dataset of ~10^6 compounds was constructed. ML models were applied to predict the photocatalytic activities of this candidate dataset. Promising photocatalysts predicted to have narrow bandgaps and HER activity were identified for synthesis and characterization.

the single base ML models used to train the metamodel. By rapidly screening a large, hypothetical materials library of >10^6 candidate photocatalysts, 20 novel non-toxic examples were identified. Two materials, $Bi_9Ti_6FeO_{27}$ and Co_2TiO_4, exhibited H_2 evolution activity under both UV and visible illumination, in good agreement with the model predictions. Two other compounds with similar bandgaps $CoTi_2O_5$ and $Cu_{0.5}Ni_{0.5}Fe_2O_4$ did not generate H_2 under illumination, also consistent with the metamodel predictions. The latent feature-property relationships captured by the ML models allowed the most important materials features to be identified. The most important features for the bandgap metamodel were radii, electronegativity, and ionization energy while for H_2 evolution four features related to group, ionization energy, and bandgap play a key role. This ML-based, computational paradigm provides a rational basis for design of potential photocatalysts for water splitting.

As a relatively new strategy for material design, current ML modeling methods significantly accelerate discovery of materials with desirable properties. The construction of the ML models requires only relatively simple and accessible features from the literature or computational models rather than deep chemical

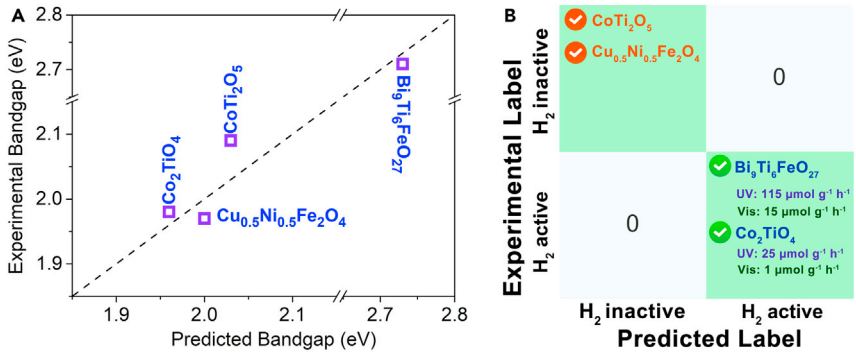

Figure 7. Photocatalysts obtained from ML model search

(A) The bandgap of the 4 selected compounds predicted by the ML model versus experimental bandgap values.

(B) Confusion matrix between true label (experimental label) and predicted label via the STC_{H2} II model.

and physical knowledge. These ML models require modest computing resources—screening of 10^6 compounds can be completed within one hour, a great saving compared to other more rigorous, physics-based computational methods. These ML models allow experimental resources to be focused on the most promising materials, thus reducing the time for design, synthesis, and characterization. The improved generalization capabilities of the metamodels generated by the stacking algorithm allows investigation of a wider range of materials and improved discovery of novel photocatalytic materials, e.g., mixed anions such as oxynitrides (Pihosh et al., 2020), oxysulfides (Wang et al., 2019a), and oxyhalides (Fujito et al., 2016) with optimal target properties. It is anticipated that an increasing number of functional materials with bespoke properties will be discovered and designed by ML modeling approaches in the future.

As we stated, there are inconsistencies in how H_2 evolution activity is reported, restricting us to classification models. Given either metadata describing the differences in experimental measurements or a standardization of the experimental protocols, it should be possible to generate robust regression models that would be more useful for identifying the most active photocatalysts for water splitting.

Limitations of the study

We built the bandgap regression model and H_2 evolution activity classification model based on small datasets using the stacking algorithm. Although the performance of these models was good, the construction and optimization of stacking models can be complicated due to the choice of base models and the optimization of the hyperparameters of each base model. Individual models, such as RF, EXT, and GBR, showed relatively good predictions on the test set, but their generalization ability was poor, probably because of insufficient training data and choice of features. Ideally, given sufficient training data and optimal features, most ML modeling algorithms may have similar predictive abilities to the stacking models.

An additional limitation is the choice of the bandgap for the most commonly reported structure rather than considering all structures and bandgaps. Accommodating these would require a method for encoding the different structural types.

STAR★METHODS

Detailed methods are provided in the online version of this paper and include the following:

- KEY RESOURCES TABLE
- RESOURCE AVAILABILITY
  - Lead contact
  - Materials availability
  - Data and code availability
- METHOD DETAILS
  - Model training data
  - Features and feature selection
  - Machine learning

- Photocatalyst synthesis
- Characterization

SUPPLEMENTAL INFORMATION

Supplemental information can be found online at https://doi.org/10.1016/j.isci.2021.103068.

ACKNOWLEDGMENTS

The authors thank Mr. Kodai Aruga, Mr. Natsutogi Iwasa, Mr. Takehiro Otsuki, Ms. Ayaka Ono, and Mr. Kanta Kobayashi for their assistance in the photocatalytic activity evaluation. The Australian Research Council is acknowledged for support through a Discovery Project (DP180103815).

AUTHOR CONTRIBUTIONS

H.M. and T.C.L. conducted the machine learning modeling. H.M. and D.C. conducted the inorganic synthesis and XRD and bandgap characterization. T.H. and K.D. performed H_2 evolution experiments. H.M., D.A.W., and R.A.C. wrote the paper. R.A.C. acquired funding, initiated, and managed the research. All authors discussed the results, reviewed, and edited the manuscript.

DECLARATION OF INTERESTS

The authors declare no competing interests.

Received: March 8, 2021
Revised: July 7, 2021
Accepted: August 25, 2021
Published: September 24, 2021

SUPPORTING CITATIONS

The following references appear in the supplemental information: Anderson et al., 2019; Asai et al., 2014; Castelli et al., 2013; Goto et al., 2018; Ishihara et al., 1999; Ishii et al., 2004; Khanahmadzadeh et al., 2015; Kim et al., 2005; Konta et al., 2003; Maeda, 2014; Masanobu et al., 2008; Ogura et al., 1997; Sahoo and Maggard, 2013; Sakata et al., 2016; Sato et al., 2003; Subbanna et al., 1990; Velinov et al., 2013; Yang et al., 2009; Yang et al., 2017; Yuan et al., 2010; Zhang et al., 2010; Zhang et al., 2012; Zhou et al., 2017.

REFERENCES

Adak, M.K., Das, A., and Dhak, D. (2020). Observation of eectrical and energy storage properties of lead-free transition metal-doped $BaBi_2(NbTa)O_9$ nanoceramics prepared through chemical route. J. Mater. Sci. *31*, 6786–6795.

Alexander, D.L.J., Tropsha, A., and Winkler, D.A. (2015). Beware of R2: simple, unambiguous assessment of the prediction accuracy of QSAR and QSPR models. J. Chem. Inf. Model. *55*, 1316–1322.

Anderson, K.P., Giri, A.K., Vinci, R.P., and Chan, H.M. (2019). Single crystal growth of $CoTi_2O_5$ by solid state reaction synthesis. J. Am. Ceram. Soc. *102*, 5050–5062.

Asai, R., Nemoto, H., Jia, Q., Saito, K., Iwase, A., and Kudo, A. (2014). A visible light responsive rhodium and antimony-codoped $SrTiO_3$ powdered photocatalyst loaded with an IrO_2 cocatalyst for solar water splitting. Chem. Commun. *50*, 2543–2546.

Bai, W., Xu, W.F., Wu, J., Zhu, J.Y., Chen, G., Yang, J., Lin, T., Meng, X.J., Tang, X.D., and Chu, J.H. (2012). Investigations on electrical, magnetic and optical behaviors of five-layered aurivillius $Bi_6Ti_3Fe_2O_{18}$ polycrystalline films. Thin Solid Films *525*, 195–199.

Bouzidi, A., Benramdane, N., Medles, M., Khadraoui, M., Bresson, S., Mathieu, C., Desfeux, R., and Marssi, M.E. (2010). Synthesis of $LiVO_3$ thin films by spray pyrolysis technique. J. Alloys Compd. *503*, 445–448.

Butler, K.T., Davies, D.W., Cartwright, H., Isayev, O., and Walsh, A. (2018). Machine learning for molecular and materials science. Nature *559*, 547–555.

Can, E., and Yildirim, R. (2019). Data mining in photocatalytic water splitting over perovskites literature for higher hydrogen production. Appl. Catal. B Environ. *242*, 267–283.

Castelli, I.E., Jacobsen, K.W., and Thygesen, K. (2013). Computational Screening of Materials for Water Splitting Applications (Technical University of Denmark (DTU)).

Castelli, I.E., Hüser, F., Pandey, M., Li, H., Thygesen, K.S., Seger, B., Jain, A., Persson, K.A., Ceder, G., and Jacobsen, K.W. (2015). New light-harvesting materials using accurate and efficient bandgap calculations. Adv. Energy Mater. *5*, 1400915.

Chanussot, L., Das, A., Goyal, S., Lavril, T., Shuaibi, M., Riviere, M., Tran, K., Heras-Domingo, J., Ho, C., Hu, W., et al. (2021). Open catalyst 2020 (OC20) dataset and community challenges. ACS Catal. *11*, 6059–6072.

Chatzimparmpas, A., Martins, R.M., Kucher, K., and Kerren, A. (2021). StackGenVis: alignment of data, algorithms, and models for stacking ensemble learning using performance metrics. IEEE Trans. Vis. Comput. Graph. *27*, 1547–1557.

Chen, S., Takata, T., and Domen, K. (2017). Particulate photocatalysts for overall water splitting. Nat. Rev. Mater. *2*, 17050.

Chen, H., Song, L., Ouyang, S., Wang, J., Lv, J., and Ye, J. (2019). Co and Fe codoped $WO_{2.72}$ as alkaline-solution-available oxygen evolution reaction catalyst to construct photovoltaic water splitting system with solar-to-hydrogen efficiency of 16.9%. Adv. Sci. *6*, 1900465.

Chen, C., Zuo, Y., Ye, W., Li, X., Deng, Z., and Ong, S.P. (2020). A critical review of machine learning of energy materials. Adv. Energy Mater. *10*, 1903242.

Davies, D.W., Butler, K.T., Jackson, A.J., Morris, A., Frost, J.M., Skelton, J.M., and Walsh, A. (2016). Computational screening of all stoichiometric inorganic materials. Chem *1*, 617–627.

Fanourgakis, G.S., Gkagkas, K., Tylianakis, E., and Froudakis, G.E. (2020). A universal machine learning algorithm for large-scale screening of materials. J. Am. Chem. Soc. *142*, 3814–3822.

Fathinia, M., Khataee, A., Aber, S., and Naseri, A. (2016). Development of kinetic models for photocatalytic ozonation of phenazopyridine on TiO_2 nanoparticles thin flm in a mixed semi-batch photoreactor. Appl. Catal. B Environ. *184*, 270–284.

Fujishima, A., and Honda, K. (1972). Electrochemical photolysis of water at a semiconductor electrode. Nature *238*, 37–38.

Fujito, H., Kunioku, H., Kato, D., Suzuki, H., Higashi, M., Kageyama, H., and Abe, R. (2016). Layered perovskite oxychloride Bi_4NbO_8Cl: a stable visible light responsive photocatalyst for water splitting. J. Am. Chem. Soc. *138*, 2082–2085.

Furlan, C., and Mortarino, C. (2018). Forecasting the impact of renewable energies in competition with non-renewable sources. Renew. Sustain. Energy Rev. *81*, 1879–1886.

Ghasemian, A., Hosseinmardi, H., Galstyan, A., Airoldi, E.M., and Clauset, A. (2020). Stacking models for nearly optimal link prediction in complex networks. Proc. Natl. Acad. Sci. U S A *117*, 23393–23400.

Gómez-Bombarelli, R., Aguilera-Iparraguirre, J., Hirzel, T.D., Duvenaud, D., Maclaurin, D., Blood-Forsythe, M.A., Chae, H.S., Einzinger, M., Ha, D.-G., Wu, T., et al. (2016). Design of efficient molecular organic light-emitting diodes by a high-throughput virtual screening and experimental approach. Nat. Mater. *15*, 1120–1127.

Goto, Y., Hisatomi, T., Wang, Q., Higashi, T., Ishikiriyama, K., Maeda, T., Sakata, Y., Okunaka, S., Tokudome, H., Katayama, M., et al. (2018). A particulate photocatalyst water-splitting panel for large-scale solar hydrogen generation. Joule *2*, 509–520.

Green, M.A., and Bremner, S.P. (2017). Energy conversion approaches and materials for high-efficiency photovoltaics. Nat. Mater. *16*, 23–34.

Gu, G.H., Noh, J., Kim, I., and Jung, Y. (2019). Machine learning for renewable energy materials. J. Mater. Chem. A *7*, 17096–17117.

Himanen, L., Geurts, A., Foster, A.S., and Rinke, P. (2019). Data-driven materials science: status, challenges, and perspectives. Adv. Sci. *6*, 1900808.

Ishihara, T., Nishiguchi, H., Fukamachi, K., and Takita, Y. (1999). Effects of acceptor doping to $KTaO_3$ on photocatalytic decomposition of pure H_2O. J. Phys. Chem. B *103*, 1–3.

Ishii, T., Kato, H., and Kudo, A. (2004). H_2 evolution from an aqueous methanol solution on $SrTiO_3$ photocatalysts codoped with chromium and tantalum ions under visible light irradiation. J. Photochem. Photobiol. A Chem. *163*, 181–186.

Jain, A., Ong, S.P., Hautier, G., Chen, W., Richards, W.D., Dacek, S., Cholia, S., Gunter, D., Skinner, D., Ceder, G., and Persson, K.A. (2013). Commentary: the materials project: a materials genome approach to accelerating materials innovation. APL Mater. *1*, 011002.

Janet, J.P., Duan, C., Yang, T., Nandy, A., and Kulik, H.J. (2019). A quantitative uncertainty metric controls error in neural network-driven chemical discovery. Chem. Sci. *10*, 7913–7922.

Jordan, M.I., and Mitchell, T.M. (2015). Machine learning: trends, perspectives, and prospects. Science *349*, 255–260.

Kannan, N., and Vakeesan, D. (2016). Solar energy for future world: - a review. Renew. Sustain. Energy Rev. *62*, 1092–1105.

Khanahmadzadeh, S., Enhessari, M., Solati, Z., Mohebalizadeh, A., and Alipouramjad, A. (2015). Synthesis, characterization and optical band gap of the Co_2TiO_4 nanoparticles. Mater. Sci. Semicond. Process. *31*, 599–603.

Kim, J., Hwang, D.W., Kim, H.G., Bae, S.W., Lee, J.S., Li, W., and Oh, S.H. (2005). Highly efficient overall water splitting through optimization of preparation and operation conditions of layered perovskite photocatalysts. Top. Catal. *35*, 295–303.

Konta, R., Kato, H., Kobayashi, H., and Kudo, A. (2003). Photophysical properties and photocatalytic activities under visible light irradiation of silver vanadates. Phys. Chem. Chem. Phys. *5*, 3061–3065.

Kudo, A., and Miseki, Y. (2009). Heterogeneous photocatalyst materials for water splitting. Chem. Soc. Rev. *38*, 253–278.

Le, T., Epa, V.C., Burden, F.R., and Winkler, D.A. (2012). Quantitative structure–property relationship modeling of diverse materials properties. Chem. Rev. *112*, 2889–2919.

Lee, D.K., and Choi, K.-S. (2018). Enhancing long-term photostability of $BiVO_4$ photoanodes for solar water splitting by tuning electrolyte composition. Nat. Energy *3*, 53–60.

Li, J., Pradhan, B., Gaur, S., and Thomas, J. (2019). Predictions and strategies learned from machine learning to develop high-performing perovskite solar cells. Adv. Energy Mater. *9*, 1901891.

Li, C., Hao, H., Xu, B., Zhao, G., Chen, L., Zhang, S., and Liu, H. (2020a). A progressive learning method for predicting the band gap of ABO_3 perovskites using an instrumental variable. J. Mater. Chem. C *8*, 3127–3136.

Li, H., Wang, H., Gao, Q., Han, B., Xia, K., and Zhou, C. (2020b). Hierarchical flower-like Co_2TiO_4 nanosheets with unique structural and compositional advantages to boost peroxymonosulfate activation for degradation of organic pollutants. J. Mater. Chem. A *8*, 20953–20962.

Lu, S., Zhou, Q., Ouyang, Y., Guo, Y., Li, Q., and Wang, J. (2018). Accelerated discovery of stable lead-free hybrid organic-inorganic perovskites via machine learning. Nat. Commun. *9*, 3405.

Lu, S., Zhou, Q., Ma, L., Guo, Y., and Wang, J. (2019). Rapid discovery of ferroelectric photovoltaic perovskites and material descriptors via machine learning. Small Methods *3*, 1900360.

Ma, Z., Wang, P., Gao, Z., Wang, R., and Khalighi, K. (2018). Ensemble of machine learning algorithms using the stacked generalization approach to estimate the warfarin dose. PLoS One *13*, e0205872.

van der Maaten, L., and Hinton, G. (2008). Visualizing Data using t-SNE. J. Mach. Learn. Res. *9*, 2579–2605.

Maeda, K. (2014). Rhodium-doped barium titanate perovskite as a stable p-type semiconductor photocatalyst for hydrogen evolution under visible light. ACS Appl. Mater. Interfaces *6*, 2167–2173.

Maeda, K., Hirayama, N., Nakata, H., Wakayama, H., and Oka, K. (2020). Oxyfluoride $Pb_2Ti_4O_9F_2$ as a stable anode material for photoelectrochemical water oxidation. J. Phys. Chem. C *124*, 1844–1850.

Masanobu, H., Ryu, A., Hideki, S., and Kazunari, D. (2008). Photocatalytic water splitting into H_2 and O_2 over titanate pyrochlores $Ln_2Ti_2O_7$ (Ln = Lanthanoid: Eu–Lu). Bull. Chem. Soc. Jpn. *81*, 1315–1321.

Masood, H., Toe, C.Y., Teoh, W.Y., Sethu, V., and Amal, R. (2019). Machine learning for accelerated discovery of solar photocatalysts. ACS Catal. *9*, 11774–11787.

Meinshausen, M., Meinshausen, N., Hare, W., Raper, S.C.B., Frieler, K., Knutti, R., Frame, D.J., and Allen, M.R. (2009). Greenhouse-gas emission targets for limiting global warming to 2 °C. Nature *458*, 1158–1162.

Nursam, N.M., Wang, X., and Caruso, R.A. (2015). High-throughput synthesis and screening of titania-based photocatalysts. ACS Comb. Sci. *17*, 548–569.

Ogura, S., Kohno, M., Sato, K., and Inoue, Y. (1997). Photocatalytic activity for water decomposition of RuO_2-combined $M_2Ti_6O_{13}$ (M = Na, K, Rb, Cs). Appl. Surf. Sci. *121-122*, 521–524.

Pan, L., Kim, J.H., Mayer, M.T., Son, M.-K., Ummadisingu, A., Lee, J.S., Hagfeldt, A., Luo, J., and Grätzel, M. (2018). Boosting the performance of Cu_2O photocathodes for unassisted solar water splitting devices. Nat. Catal. *1*, 412–420.

Pihosh, Y., Nandal, V., Minegishi, T., Katayama, M., Yamada, T., Seki, K., Sugiyama, M., and Domen, K. (2020). Development of a core–shell heterojunction Ta_3N_5-nanorods/$BaTaO_2N$ photoanode for solar water splitting. ACS Energy Lett. *5*, 2492–2497.

Rajan, A.C., Mishra, A., Satsangi, S., Vaish, R., Mizuseki, H., Lee, K.-R., and Singh, A.K. (2018). Machine-learning-assisted accurate band gap predictions of functionalized MXene. Chem. Mater. *30*, 4031–4038.

Ren, F., Ward, L., Williams, T., Laws, K.J., Wolverton, C., Hattrick-Simpers, J., and Mehta, A. (2018). Accelerated discovery of metallic glasses through iteration of machine learning and high-throughput experiments. Sci. Adv. *4*, eaaq1566.

Sahoo, P.P., and Maggard, P.A. (2013). Crystal chemistry, band engineering, and photocatalytic activity of the $LiNb_3O_8$–$CuNb_3O_8$ solid solution. Inorg. Chem. *52*, 4443–4450.

Sakata, Y., Miyoshi, Y., Maeda, T., Ishikiriyama, K., Yamazaki, Y., Imamura, H., Ham, Y., Hisatomi, T., Kubota, J., Yamakata, A., and Domen, K. (2016). Photocatalytic property of metal ion added $SrTiO_3$ to overall H_2O splitting. Appl. Catal. A Gen. *521*, 227–232.

Sanchez-Lengeling, B., and Aspuru-Guzik, A. (2018). Inverse molecular design using machine learning: generative models for matter engineering. Science *361*, 360–365.

Sato, J., Saito, N., Nishiyama, H., and Inoue, Y. (2003). Photocatalytic activity for water decomposition of indates with octahedrally coordinated d^{10} configuration. I. Influences of preparation conditions on activity. J. Phys. Chem. B *107*, 7965–7969.

Singh, S.K., Bejagam, K.K., An, Y., and Deshmukh, S.A. (2019). Machine-learning based stacked ensemble model for accurate analysis of molecular dynamics simulations. J. Phys. Chem. A *123*, 5190–5198.

Subbanna, G.N., Row, T.N.G., and Rao, C.N.R. (1990). Structure and dielectric properties of recurrent intergrowth structures formed by the Aurivillius family of bismuth oxides of the formula $Bi_2A_{n-1}B_nO_{3n+3}$. J. Solid State Chem. *86*, 206–211.

Sun, Y., Liao, H., Wang, J., Chen, B., Sun, S., Ong, S.J.H., Xi, S., Diao, C., Du, Y., Wang, J.-O., et al. (2020). Covalency competition dominates the water oxidation structure–activity relationship on spinel oxides. Nat. Catal. *3*, 554–563.

Tabor, D.P., Roch, L.M., Saikin, S.K., Kreisbeck, C., Sheberla, D., Montoya, J.H., Dwaraknath, S., Aykol, M., Ortiz, C., Tribukait, H., et al. (2018). Accelerating the discovery of materials for clean energy in the era of smart automation. Nat. Rev. Mater. *3*, 5–20.

Tachibana, Y., Vayssieres, L., and Durrant, J.R. (2012). Artificial photosynthesis for solar water-splitting. Nat. Photon. *6*, 511–518.

Toyao, T., Maeno, Z., Takakusagi, S., Kamachi, T., Takigawa, I., and Shimizu, K.-i. (2020). Machine learning for catalysis informatics: recent applications and prospects. ACS Catal. *10*, 2260–2297.

Vavilapalli, D.S., Srikanti, K., Mannam, R., Tiwari, B., K, M.K., Rao, M.S.R., and Singh, S. (2018). Photoactive brownmillerite multiferroic $KBiFe_2O_5$ and its potential application in sunlight-driven photocatalysis. ACS Omega *3*, 16643–16650.

Velinov, N., Koleva, K., Tsoncheva, T., Manova, E., Paneva, D., Tenchev, K., Kunev, B., and Mitov, I. (2013). Nanosized $Cu_{0.5}Co_{0.5}Fe_2O_4$ ferrite as catalyst for methanol decomposition: effect of preparation procedure. Catal. Commun. *32*, 41–46.

Wang, R. (2018). Significantly improving the prediction of molecular atomization energies by an ensemble of machine learning algorithms and rescanning input space: a stacked generalization approach. J. Phys. Chem. C *122*, 8868–8873.

Wang, Q., and Domen, K. (2020). Particulate photocatalysts for light-driven water splitting: mechanisms, challenges, and design strategies. Chem. Rev. *120*, 919–985.

Wang, C.S., and Pickett, W.E. (1983). Density-functional theory of excitation spectra of semiconductors: application to Si. Phys. Rev. Lett. *51*, 597–600.

Wang, W., Chen, J., Li, C., and Tian, W. (2014). Achieving solar overall water splitting with hybrid photosystems of photosystem II and artificial photocatalysts. Nat. Commun. *5*, 4647.

Wang, Y., Suzuki, H., Xie, J., Tomita, O., Martin, D.J., Higashi, M., Kong, D., Abe, R., and Tang, J. (2018). Mimicking natural photosynthesis: solar to renewable H_2 fuel synthesis by Z-scheme water splitting systems. Chem. Rev. *118*, 5201–5241.

Wang, W., Tadé, M.O., and Shao, Z. (2015). Research progress of perovskite materials in photocatalysis- and photovoltaics-related energy conversion and environmental treatment. Chem. Soc. Rev. *44*, 5371–5408.

Wang, F.G., Young, S.M., Zheng, F., Grinberg, I., and Rappe, A.M. (2016). Substantial bulk photovoltaic effect enhancement via nanolayering. Nat. Commun. *7*, 10419.

Wang, Q., Nakabayashi, M., Hisatomi, T., Sun, S., Akiyama, S., Wang, Z., Pan, Z., Xiao, X., Watanabe, T., Yamada, T., et al. (2019a). Oxysulfide photocatalyst for visible-light-driven overall water splitting. Nat. Mater. *18*, 827–832.

Wang, Z., Li, C., and Domen, K. (2019b). Recent developments in heterogeneous photocatalysts for solar-driven overall water splitting. Chem. Soc. Rev. *48*, 2109–2125.

Wheeler, G.P., and Choi, K.-S. (2018). Investigation of p-type $Ca_2Fe_2O_5$ as a photocathode for use in a water splitting photoelectrochemical cell. ACS Appl. Energy Mater. *1*, 4917–4923.

Wolpert, D.H. (1992). Stacked generalization. Neural Netw. *5*, 241–259.

Wu, M., Tian, Z., Yuan, S., and Huang, Z. (2012). Magnetic and optical properties of the aurivillius phase $Bi_5Ti_3FeO_{15}$. Mater. Lett. *68*, 190–192.

Wu, Y., Lazic, P., Hautier, G., Persson, K., and Ceder, G. (2013). First principles high throughput screening of oxynitrides for water-splitting photocatalysts. Energy Environ. Sci. *6*, 157–168.

Wu, M., Lou, X., Li, T., Li, J., Wang, S., Li, W., Peng, B., and Gou, G. (2017). Ni-doped $SrBi_2Nb_2O_9$ – perovskite oxides with reduced band gap and stable ferroelectricity for photovoltaic applications. J. Alloys Compd. *724*, 1093–1100.

Yang, Y., Chen, Q., Yin, Z., and Li, J. (2009). Study on the photocatalytic activity of $K_2La_2Ti_3O_{10}$ doped with vanadium (V). J. Alloys Compd. *488*, 364–369.

Yang, J., Jiang, P., Yue, M., Yang, D., Cong, R., Gao, W., and Yang, T. (2017). $Bi_2Ga_4O_9$: an undoped single-phase photocatalyst for overall water splitting under visible light. J. Catal. *345*, 236–244.

Zhang, H., Chen, G., He, X., and Xu, J. (2012). Electronic structure and photocatalytic properties of Ag–La codoped $CaTiO_3$. J. Alloys Compd. *516*, 91–95.

Zhang, H., Chen, G., and Li, X. (2009). Synthesis and visible light photocatalysis water splitting property of chromium-doped $Bi_4Ti_3O_{12}$. Solid State Ionics *180*, 1599–1603.

Yuan, Y., Zhao, Z., Zheng, J., Yang, M., Qiu, L., Li, Z., and Zou, Z. (2010). Polymerizable complex synthesis of $BaZr_{1-x}Sn_xO_3$ photocatalysts: role of Sn^{4+} in the band structure and their photocatalytic water splitting activities. J. Mater. Chem. *20*, 6772–6779.

Zhang, H., Chen, G., Li, Y., and Teng, Y. (2010). Electronic structure and photocatalytic properties of copper-doped $CaTiO_3$. Int. J. Hydrogen Energy *35*, 2713–2716.

Zhang, G., Liu, G., Wang, L., and Irvine, J.T.S. (2016). Inorganic perovskite photocatalysts for solar energy utilization. Chem. Soc. Rev. *45*, 5951–5984.

Zhang, X., Zhang, Z., Wu, D., Zhang, X., Zhao, X., and Zhou, Z. (2018). Computational screening of 2D materials and rational design of heterojunctions for water splitting photocatalysts. Small Methods *2*, 1700359.

Zhou, M., Zu, X.T., Sun, K., Liu, W., and Xiang, X. (2017). Enhanced photocatalytic hydrogen generation of nano-sized mesoporous $InNbO_4$ crystals synthesized via a polyacrylamide gel route. Chem. Eng. J. *313*, 99–108.

Zhu, S., and Wang, D. (2017). Photocatalysis: basic principles, diverse forms of implementations and emerging scientific opportunities. Adv. Energy Mater. *7*, 1700841.

Zhuo, Y., Mansouri Tehrani, A., Oliynyk, A.O., Duke, A.C., and Brgoch, J. (2018). Identifying an efficient, thermally robust inorganic phosphor host via machine learning. Nat. Commun. *9*, 4377.

STAR★METHODS

KEY RESOURCES TABLE

REAGENT or RESOURCE	SOURCE	IDENTIFIER
Chemicals, peptides, and recombinant proteins		
Bismuth(III) nitrate pentahydrate	Aldrich	CAS: 10035-06-0
Iron(III) nitrate nonahydrate	Aldrich	CAS: 7782-61-8
Titanium(IV) isopropoxide	Aldrich	CAS: 546-68-9
Ethanol	Supelco	CAS: 64-17-5
Sodium Hydroxide	Chem-supply	CAS: 1310-73-2
Copper(II) nitrate trihydrate	Aldrich	CAS: 10031-43-3
Nickel(II) nitrate hexahydrate	Aldrich	CAS: 13478-00-7
Cobalt(II) nitrate hexahydrate	Aldrich	CAS: 10026-22-9
Software and algorithms		
scikit-learn	Open-source	https://scikit-learn.org/stable/
Mlxtend	Open-source	http://rasbt.github.io/mlxtend/
Other		
Bruker D4 Endeavor powder X-ray diffractometer	Bruker	https://www.brukersupport.com/ProductDetail/732
Agilent Cary 5000 spectrophotometer	Agilent	https://www.agilent.com/en/product/molecular-spectroscopy/uv-vis-uv-vis-nir-spectroscopy/uv-vis-uv-vis-nir-systems/cary-5000-uv-vis-nir
Closed-circulation system	Makuhari	AU-306-T02-S2

RESOURCE AVAILABILITY

Lead contact

Further information and requests for resources should be directed to Rachel Caruso (rachel.caruso@rmit.edu.au).

Materials availability

There are restrictions to the availability of the photocatalysts as we do not stock excess synthesized materials. The materials can be prepared as described in the Experimental Procedure.

Data and code availability

The data for this study are available within the article and the supplemental information, or from publicly accessible databases (The Materials Project). Any additional information required to reanalyze the data reported in this paper is available from the lead contact upon request.

METHOD DETAILS

Model training data

The performance of ML models depends on the size and diversity of the training data (Butler et al., 2018; Chen et al., 2020; Le et al., 2012). Two datasets of diverse photocatalytic metal oxides were compiled: one used to train regression models to predict bandgaps, the other for H_2 evolution classification model training. 489 oxides with experimental optical bandgap values (Table S9 BG dataset related to STAR Methods) were extracted from the literature, of which 380 oxides have binary H_2 evolution data (Table S10 H2 dataset related to STAR Methods, active = H_2 evolution, inactive = no H_2 evolution). The two

datasets have been included as supplemental information. The BG dataset (Table S9 BG dataset related to STAR Methods) was composed of oxides with diverse structures that had been reported to be photocatalytically active, including perovskite (46%), pyrochlore (15%), ilmenite (8%), scheelite (10%), spinel (5%), trirutile (2%), brannerite (2%), delafossite (2%) and others, as can be seen in the dataset (supplemental information). Photocatalysts likely to split water using visible light activity required bandgaps of 2.0 – 2.7 eV. 33% of the compounds in the BG dataset (Table S9 BG Dataset related to STAR Methods) were in this range.

As the preparation method can influence HER activity, we defined materials as HER active if at least one article reported photocatalytic H_2 evolution, and inactive when its reported conduction band minimum is positive and no article reported photocatalytic H_2 production. All oxides can be represented by a general formula $A_xA'_{n-x}B_yB'_{m-y}O_l$ ($x>0$, $x \geq n-x$, $y>0$, $y \geq m-y$, $l>0$), where A/A' and B/B' are elements with similar properties that always reside in identical sites of a compound. Here, we classified the metal elements of the oxides as A or B according to their structure. For example, in perovskites (ABO_3) a B element is a smaller six-coordinate ion, and an A element is a larger twelve-coordinate ion. In spinels (AB_2O_4) cations A and B occupy the octahedral and tetrahedral sites in the lattice, respectively. The sequences of A/A' and B/B' were determined following these rules: 1) the amounts of A (n_A) and B (n_B) were larger than A' ($n_{A'}$) and B' ($n_{B'}$); 2) when $n_A = n_{A'}$ or $n_B = n_{B'}$, the periods of A and B were smaller than A' and B'; 3) when both the amount and periods of A/A' and B/B' were equal, the groups of A (G_A) and B (G_B) were smaller than A' ($G_{A'}$) and B' ($G_{B'}$). Given that the bandgaps of some compounds vary due to differences in structure, only the bandgap for the most frequently reported structure was used in the photocatalysis data set. For example, only the monoclinic $BiVO_4$ phase was considered (bandgap 2.4 eV), rather than the tetragonal and orthorhombic $BiVO_4$ forms.

The cation elements of these oxides cover a large part of the periodic table (40 types of A and A' elements, and 30 types of B and B' elements). Thus, ML models trained on these datasets should generalize well to new materials.

Features and feature selection

The materials in the dataset were described by chemical features (descriptors) obtained from materials handbooks and databases. The choice of features is important as it is one of the main factors (along with data quantity, quality, and diversity) determining model quality. Although many features may correlate with the target properties, the number of features must be limited to avoid overfitting and degradation of model predictivity by the presence of low relevance features (noise). Large numbers of descriptors also increase the complexity of the model, increasing the computation expense and compromising model predictivity and interpretability (Le et al., 2012). Feature selection was therefore employed to remove redundant and uninformative features, and this relevant subset of features was used to train and test a series of ML models.

Simple, basic atomic and physicochemical features were calculated for the dataset (Lu et al., 2019). Each component of the photocatalysts (A, A', B, B') was described by 14 features obtained from the periodic table, materials handbooks, and material databases (Table S1) (Li et al., 2019, 2020a; Lu et al., 2019; Rajan et al., 2018). To refine the number of features to the most relevant subset the full descriptor set of 57 features (56 features related to A, A', B and B', while n_x is the amount of O) was subjected to feature selection. To ensure the derived ML models can be extended to mixed-anion photocatalysts (e.g., $A_xA'_{n-x}B_yB'_{m-y}O_lX_{l-z}$), the anion elements O and X can also be described by the same 14 features. In this work, however, we focussed on the photocatalytic oxides.

The initial set of 57 features were pruned by removing those with low variance, and those highly correlated with other features using Pearson correlation coefficients (Figure S1). The remaining features were ranked by the GBR algorithm according to their relative importance and the least important feature removed. This process is repeated and the model score (R^2) of trained ML model at each step used to identify the feature subset with the best performance (Figure S2 and Table S2). After this process, the optimal subset contained 29 features. This optimal feature set consists of the group number in the periodic table (G), Van der Waals radii (R), valence (V), electronegativity (X), ionization energy (E), polarizability (P) for all metal elements, and the mole fraction (n) of metal elements and oxygen.

Machine learning

The datasets are randomly split into a training set (80%) and test set (20%) (Le et al., 2012). The supervised ML regression models for predicting the bandgap of photocatalysts were trained on the BG training set (391 photocatalysts, 80% of the 489 photocatalysts in BG dataset). The supervised classification models for predicting HER activity of photocatalysts were trained on the H_2 training set (304 photocatalysts, 80% of the 380 photocatalysts with HER activity reported from the literature). The test sets were only used for testing the performance of the ML models, and were not involved in any training processes. The base ML models were generated by these algorithms: SVR; SVC; RF; LASSO; ridge regression, EXT; GBR; GBT; and Bagging from the open-source scikit-learn package. The base models were optimized by grid searching methods (5-fold cross validation on training set, the optimized hypermeters were listed in Tables S3 and S4), and then 5-fold cross validation was conducted on the training set to generate five models for each algorithm for the base level of the stacking model (Figure 2). The stacking algorithm meta-models were constructed using the open source mlxtend package. Again, for the stacking models, the combination of the base models, and selection of the meta-model, were also optimized by grid searches (5-fold cross validation on training set, the optimized hypermeters were listed in Tables S3 and S4).

Photocatalyst synthesis

The four compounds of interest identified by the ML models were $Bi_9Ti_6FeO_{27}$, Co_2TiO_4, $CoTi_2O_5$, and $Cu_{0.5}Ni_{0.5}Fe_2O_4$. $Bi_9Ti_6FeO_{27}$ and $Cu_{0.5}Ni_{0.5}Fe_2O_4$ were synthesized by hydrothermal methods, while Co_2TiO_4 and $CoTi_2O_5$ were synthesized by co-precipitation.

$Bi_9Ti_6FeO_{27}$. $Bi(NO_3)_3 \cdot 5H_2O$ (2.0 mmol, Aldrich, 98%) and $Fe(NO_3)_3 \cdot 9H_2O$ (0.22 mmol, Aldrich, 98%) were dissolved in MilliQ water (30 mL), while titanium(IV) isopropoxide (1.33 mmol, Aldrich, 97%) was quickly added to ethanol (10 mL, Supelco, 99%). These two solutions were then mixed, and the pH value of the solution was adjusted to 11 with the dropwise addition of NaOH (2.5 M, Chem-supply, 98%). After 30 min vigorous stirring, the as-prepared mixture was transferred into a 50 mL Teflon-lined autoclave and heated at 180°C for 24 h. After the solvothermal treatment, precipitates were separated by centrifugation, and washed with deionized water and ethanol 3 times, followed by drying at 60°C in air overnight. The dried samples were then calcined in a furnace at 700°C for 15 min in air.

$Cu_{0.5}Ni_{0.5}Fe_2O_4$. $Cu(NO_3)_2 \cdot 3H_2O$ (1.0 mmol, Aldrich, 98%), $Ni(NO_3)_2 \cdot 6H_2O$ (1.0 mmol, Aldrich, 98.5%), and $Fe(NO_3)_3 \cdot 9H_2O$ (2.0 mmol, Aldrich, 98%) were dissolved in MilliQ water (30 mL). The pH value of the solution was adjusted to 11 with the dropwise addition of NaOH (2.5 M, Chem-supply, 98%). After 30 min vigorous stirring, the as-prepared mixture was transferred into a 50 mL Teflon-coated autoclave and heated to 180°C for 24 h. After the hydrothermal treatment, precipitates were separated by centrifugation, and washed with deionized water and ethanol 3 times, followed by drying at 60°C in air overnight.

Co_2TiO_4. $Co(NO_3)_2 \cdot 6H_2O$ (2.0 mmol, Aldrich, 98%) was dissolved in MilliQ water (30 mL), while titanium(IV) isopropoxide (1.0 mmol, Aldrich, 97%) was quickly added into ethanol (10 mL, Supelco, 99%). These two solutions were then mixed, and the pH value of the solution was adjusted to 11 with the dropwise addition of NaOH (2.5 M, Chem-supply, 98%). After 60 min vigorous stirring, precipitates were separated by centrifugation, and washed with deionized water and ethanol 3 times, followed by drying at 60°C in air overnight. The dried samples were then calcined in a furnace at 850°C for 4 h in air.

$CoTi_2O_5$. $Co(NO_3)_2 \cdot 6H_2O$ (1.0 mmol, Aldrich, 98%) was dissolved in MilliQ water (30 mL), while titanium(IV) isopropoxide (2.0 mmol, Aldrich, 97%) was quickly added into ethanol (10 mL, Supelco, 99%). These two solutions were then mixed, and the pH value of the solution was adjusted to 11 with the dropwise addition of NaOH (2.5 M, Chem-supply, 98%). After 60 min vigorous stirring, precipitates were separated by centrifugation, and washed with deionized water and ethanol several times, followed by drying at 60°C in air overnight. The dried samples were then calcined in a furnace at 1150°C for 6 h in air.

Characterization

The crystalline phases of the synthesized photocatalysts were investigated using a Bruker D4 Endeavor powder X-ray diffractometer (XRD) with Cu Kα radiation. The samples were scanned from 10 to 75° in 2θ

at a step size of 0.02°. UV–visible-near infrared (UV–vis-NIR) reflection spectra were measured on an Agilent Cary 5000 spectrophotometer equipped with a Harrick Praying Mantis accessory. The photocatalytic H_2 evolution was carried out with 0.2 g photocatalyst (loading 0.1 wt% Pt as cocatalyst by photodeposition) suspended in a 200 mL aqueous methanol solution (10 vol%) in a Pyrex glass reaction cell. The reaction cell was connected to a gas-closed system with a gas-circulated pump. A 300-W Xe arc lamp was employed for the light source of the photocatalytic reaction. The reaction system was degassed by evacuation and then filled with 10 kPa Ar. During the visible-light reaction ($400\ nm < \lambda < 800\ nm$), a L42 cut-off filter was used to remove UV light.